Dalton Transactions

Accepted Manuscript

ROYAL SOCIETY OF CHEMISTRY

www.rsc.org/dalton

Triazolate-based 3D frameworks and 2D layer with centrosymmetric Cu^{II}_7, Cu^{II}_5, Cu^{II}_4 clusters and tunable interlayer/interchain compactness: Hydrothermal syntheses, crystal structures and magnetic properties

Yuan-Yuan Zhang,[a] Hong Zhao,[a] En-Cui Yang,[a, *] Zhong-Yi Liu,[a] Qiu Shang[a] and Xiao-Jun Zhao [a, b *]

To *Dalton Trans* (Article)

[a] *College of Chemistry*, *Key Laboratory of Inorganic-Organic Hybrid Functional Material Chemistry*, *Ministry of Education*, *Tianjin Key Laboratory of Structure and Performance for Functional Molecules*, *Tianjin Normal University*, *Tianjin 300387*, *P. R. China*. E-mail: encui_yang@163.com, *xiaojun_zhao15@163.com; Fax:+86-22-23766556*

[b] *Collaborative Innovation Center of Chemical Science and Engineering (Tianjin), Tianjin 300071, China*

† Electronic supplementary information (ESI) available: Selected bond lengths and angles, additional figures, PXRD patterns, TG curves, magnetic results and X-ray crystallographic files in CIF format for **1**–**4**. CCDC 1013117–1013120 for **1**–**4**. For ESI and crystallographic data in CIF or other electronic format see DOI:10.1039/

Four 1,2,3-triazolate-based coordination polymers (CPs) with varied dimensionality, different nuclearity numbers and core topologies, $[Cu_4(\mu\text{-OH})(\mu_3\text{-OH})(ta)_2(btec)]_n$ (**1**), $\{[Cu_6(\mu_3\text{-OH})_2(ta)_8(tp)]\cdot 2.5H_2O\}_n$ (**2**), $\{[Cu_5((\mu_3\text{-OH})_2(ta)_4(ip)_2]\cdot 2H_2O\}_n$ (**3**) and $\{[Cu_5(\mu\text{-OH})_2(\mu_3\text{-OH})_2(ta)_2(pa)_2]\cdot 2H_2O\}_n$ (**4**) (ta = 1,2,3-triazolate, btec = 1,2,4,5-benzenetetracarboxylate, tp = terephthalate, ip = isophthalate and pa = phthalate), were hydrothermally synthesized by varying the numbers and positions of the carboxylate group appended on the phenyl tether, and structurally and magnetically characterized. The former three entities are three-dimensional (3D) robust frameworks with a $(4^4\cdot 6^2)(4^{11}\cdot 6^5)_2(4^{13}\cdot 6^{10}\cdot 8^5)$ topological net containing centrosymmetric Cu^{II}_7 clusters, square-planar Cu^{II}_1 cores and tetratopic $btec^{4-}$ linkers for **1**, a pillared-layer structure consisting of Cu^{II}_5+Cu^{II}_1-based coplanar layers and ditopic tp^{2-} pillars for **2** as well as a microporous architecture derived from Cu^{II}_5 clusters and directional ip^{2-} connectors for **3**. By contrast, complex **4** exhibits an undulated two-dimensional (2D) layer with alternating Cu^{II}_4+Cu^{II}_1 chains interconnected by anionic pa^{2-} connectors. Crystallographically, the increment of the local nuclearity from Cu^{II}_4 up to Cu^{II}_7 in **1**–**4** benefits greatly from the synergistic co-coordination of hydroxyl group and coplanar ta^- ligand towards the metal ion, and the interlayer/interchain compactness is significantly tuned by the position isomerism of the dicarboxylate moieties. Due to the antiferromagnetic coupling in the local clusters and the asymmetric superexchange by μ_3-ta^- mediator, these complexes exhibit different spin ground states (paramagnetic $S = 1$ and 1/2, ferrimagnetic $S = 1/2$ as well as spin canting) at low temperature, which are informative for the polynuclear-based magnetic materials.

Introduction

Polynuclear metal cluster-based coordination polymers (CPs) have always attracted great interest due to their intriguing structures,[1] higher connectivity and stability[2–5] as well as tailorable chemical and physical properties in adsorption,[6–7] magnetism[8] and catalysis.[9–10] Synthetically speaking, two feasible and effective approaches have been extensively applied for the successful constructions of targeted CPs. One is design and synthesis of novel bifunctional ligands with compartmental coordination sites and appropriately programmed coordination information responsible simultaneously for core aggregation and backbone extension,[11–13] which requires subtle modifications, skillful techniques and abundant experiences of the synthetic chemists. The other one is mixed-ligand strategy from combinations of two or more commercially available chemicals respectively with densely multiple metal binding sites for nuclearity increase and separate functional groups for intercore connectivity, which is simple and comparatively restricted.[14–18] Acting as a popular ligand containing three sequent N donors in a coplanar five-membered heterocyclic ring, 1H-1,2,3-triazole (Hta) has gradually becoming one of ideal candidates for generation of pentanuclear metal clusters.[19–23] Variously recurrent metal ion-centered MZn_4 tetrahedron subunits (M = Zn, Ru, Cd, Fe, Co, Ni and Cu)[21–22, 24] and hourglass-like M^{II}_5 clusters (M = Zn, Cu and Co) composed of two corner-sharing triangles[25–29] have been previously obtained in the triazolate-based assembly systems by varying the central metal ions and reaction conditions. In particular, the conformation-flexible Cu^{II}_5 clusters can act as predesigned secondary building blocks to take part in the ongoing reaction processes in a ternary Cu^{II}-triazolate-sulfoisophthalate system, resulting in unexpected two-fold interpenetrating, pillared-layer and (4,8)-connected architectures by slight expansion of the cluster and variable intercluster connectivity.[19] Undoubtedly, the consecutive three N donors and the sterically unencumbered coplanar skeleton of the ta^- anion become the key structural factor for the formation of the diverse clusters.

Acting as polytopic connectors, on the other hand, aromatic polycarboxylate is capable of connecting the locally structural motifs into an extended network with intriguing and unexpected linkages. The number and position of the carboxylate group attached on the phenyl ring can essentially determine the dimensionality and topological structure of the resulting complexes.[30–31] However, the orienting and isomeric effects from the functional polycarboxylate groups have been scarcely investigated by far. Herein, as our continuous interest in the magnetostructural relationships of the Hta-based polymetallic cluster-derived CPs, self-assembly reactions of inorganic Cu^{II} sources and Hta in the presence of carboxylate-functionalized coligands with different numbers and positions were performed under controllable hydrothermal conditions. As a result, four interesting centrosymmetric Cu^{II}_n cluster (n = 4, 5, and 7)-based CPs including three 3D frameworks and one 2D layer were successfully obtained and characterized structurally and magnetically. Complex **1** is a complicated 4, 6, 8-trinodal topological net constructed from centrosymmetric Cu^{II}_7 cluster, square-planar Cu^{II}_1 node and tetratopic $btec^{4-}$ linkers, **2** has a pillared-layer architecture consisting of alternating Cu^{II}_5+Cu^{II}_1 cores and anionic tp^{2-} connectors and **3** exhibits a microporous structure constructed from two unique Cu^{II}_5 clusters-based coplanar layers and directional ip^{2-} pillars. By contrast, complex **4** features an undulated 2D layer with Cu^{II}_4+Cu^{II}_1 chain interconnected by bidirectional pa^{2-} connectors. Structurally, the increase of the core-number from four to seven and variations of the core-topology are significantly resulting from the synergistic co-coordination of hydroxyl group and 1,2,3-triazolate towards the metal ion, and the interchain/interlayer compactness is significantly tuned by the position isomerism of the dicarboxylate moieties. More interestingly, dominate antiferromagnetic couplings in the centrosymmetric Cu^{II}_n clusters lead to different spin ground states (paramagnetic S = 1 and 1/2 for **1** and **4**, ferrimagnetic S = 1/2 for **3** as well as spin canting for **2**) at low temperature. These significant results are helpful and informative for the design and preparation of

polynuclear metal cluster-based CPs.

Experimental

Materials and instruments

All initial chemicals were commercially purchased (Hta, 1,2,4,5-benzenetetracarboxylic acid (H_4btec), terephthalic acid (H_2tp), isophthalic acid (H_2ip) and phthalic acid (H_2pa)) were from Acros and other analytical-grade reagents were from Tianjin Chemical Reagent Factory) and used as received without further purification. Elemental analyses for C, H and N were carried out with a CE-440 (Leeman-Labs) analyzer. Fourier transform (FT) IR spectra (KBr pellets) were taken on an Avatar-370 (Nicolet) spectrometer in the range 4000–400 cm^{-1}. Thermogravimetric analysis (TGA) experiment was performed on a Shimadzu simultaneous DTG–60A compositional analysis instrument from room temperature to 800 ^oC under N_2 atmosphere at a heating rate of 5 ^oC min^{-1}. Powder X-ray diffraction (PXRD) patterns were obtained from a Bruker D8 ADVANCE diffractometer at 40 kV and 40 mA for Cu *K*α radiation (λ = 1.5406 Å), with a scan speed of 0.1 sec/step and a step size of 0.01^o in 2θ. The simulated PXRD pattern was calculated using single-crystal X-ray diffraction data and processed by the free Mercury v1.4 program provided by the Cambridge Crystallographic Data Center. Magnetic susceptibilities were acquired on a Quantum Design (SQUID) magnetometer MPMS-XL-7 with crystalline samples, in which the phase purity of the samples was determined by PXRD experiments. Diamagnetic corrections were estimated from Pascal's constants for all constituent atoms, and an experimental correction for the sample holder was also applied.

Syntheses of 1–4

$[Cu_4(\mu\text{-OH})(\mu_3\text{-OH})(ta)_2(btec)]_n$ (1). A mixture of Hta (21.0 mg, 0.3 mmol), H_4btec (25.0 mg, 0.1 mmol) and $CuCl_2 \cdot 2H_2O$ (17.0 mg, 0.1 mmol) was dissolved in doubly deionized water (15.0 mL) with constant

stirring. The resulting mixture was then transferred into a parr Teflon-lined stainless steel vessel (23.0 mL) and heated at 160 °C for 72 h under autogenous pressure. After the mixture was cooled to room temperature at a rate of 2.8 °C·h^{-1}, blue block-shaped crystals suitable for X-ray analysis were obtained directly, washed with water and dried in air (Yield: 25.0% based on Cu^{II} salt). Anal. Calcd for $C_{14}H_8Cu_4N_6O_{10}$: C, 24.93; H, 1.20; N, 12.46%. Found: C, 24.92; H, 1.21; N, 12.47%. FT-IR (KBr, cm^{-1}): 3474 (s), 3414 (s), 1616 (s), 1561 (s), 1493 (m), 1458 (m), 1425 (s), 1388 (s), 1347 (s), 1215 (m), 1152 (m), 1022 (w) 980 (m), 837 (w), 811 (m), 620 (w).

{[$Cu_6(\mu_3$-OH)$_2$(ta)$_8$(tp)]·2.5H_2O}$_n$ (2). A mixture containing Hta (21.0 mg, 0.3 mmol), H_2tp (16.6 mg, 0.1 mmol) and $Cu(NO_3)_2·3H_2O$ (72.3 mg, 0.3 mmol) was dissolved in doubly deionized water (8.0 mL), and the initial pH value of the mixture was adjusted to ca. 6.0 by triethylamine. The mixture was then transferred into a parr Teflon-lined stainless steel vessel (23.0 mL) and heated at 160 °C for 120 h under autogenous pressure. After the mixture was cooled to room temperature at a rate of 2.8 °C·h^{-1}, blue block-shaped crystals suitable for X-ray analysis were obtained directly, washed with water and dried in air (Yield: 60.0% based on Hta). Anal. Calcd for $C_{24}H_{27}Cu_6N_{24}O_{8.5}$: C, 24.66; H, 2.33; N, 28.76%. Found: C, 24.68; H, 2.30; N, 28.76%. FT-IR (KBr, cm^{-1}): 3413 (br), 1585 (s), 1550 (s), 1499 (s), 1384 (s), 1272 (w), 1211 (w), 1173 (w), 1123 (m), 1090 (m), 1017 (w), 982 (w), 801 (m), 749 (m), 713 (w), 668 (w), 538 (w), 491 (w).

{[Cu_5((μ_3-OH)$_2$(ta)$_4$(ip)$_2$]·2H_2O}$_n$ (3). A mixture containing Hta (21.0 mg, 0.3 mmol), H_2ip (16.6 mg, 0.1 mmol) and $Cu(OAc)_2·H_2O$ (40.0 mg, 0.2 mmol) was dissolved in doubly deionized water (8.0 mL), and the initial pH value of the mixture was adjusted to ca. 6.0 by triethylamine. The resulting mixture was then transferred into a parr Teflon-lined stainless steel vessel (23.0 mL) and heated at 160 °C for 96 h under autogenous pressure. After the mixture was cooled to room temperature at a rate of 2.8 °C·h^{-1}, blue

block-shaped crystals suitable for X-ray analysis were obtained directly, washed with water and dried in air (Yield: 60.0% based on Cu^{II} salt). Anal. Calcd for $C_{24}H_{22}Cu_5N_{12}O_{12}$: C, 29.17; H, 2.24; N, 17.01%. Found: C, 29.19; H, 2.21; N, 17.04%. FT-IR (KBr, cm^{-1}): 3551 (s), 3474 (s), 3413 (s), 3237 (w), 1637 (s), 1617 (s), 1563 (m), 1541 (w), 1387 (s), 1332 (w), 1269 (w), 1133 (m), 979 (w), 818 (w), 801 (w), 749 (w), 727 (w), 710 (w), 617 (m), 479 (w).

$\{[Cu_5(\mu\text{-}OH)_2(\mu_3\text{-}OH)_2(ta)_2(pa)_2]\cdot 2H_2O\}_n$ (4). A mixture containing Hta (14.0 mg, 0.2 mmol), H_2pa (16.6 mg, 0.1 mmol) and $Cu(OAc)_2\cdot H_2O$ (40.0 mg, 0.2 mmol) was dissolved in doubly deionized water (10.0 mL), and the initial pH value of the mixture was adjusted to ca. 6.0 by triethylamine. The resulting mixture was then transferred into a parr Teflon-lined stainless steel vessel (23.0 mL) and heated at 160 °C for 96 h under autogenous pressure. After the mixture was cooled to room temperature at a rate of 1.8 $^{o}C\cdot h^{-1}$, blue block-shaped crystals suitable for X-ray analysis were obtained directly, washed with water and dried in air (Yield: 40.0% based on Cu^{II} salt). Anal. Calcd for $C_{20}H_{20}Cu_5N_6O_{14}$: C, 27.11; H, 2.27; N, 9.48%. Found: C, 27.12; H, 2.25; N, 9.45%. FT-IR (KBr, cm^{-1}): 3547 (s), 3465 (s), 3421 (s), 1637 (s), 1618 (s), 1561 (s), 1478 (w), 1408 (m), 1381 (w), 1264 (m), 1223 (m), 1141 (w), 1110 (w), 960 (w), 878 (w), 827 (w), 796 (w), 749 (w), 699 (w), 612 (w), 578 (w), 496 (w), 420 (w).

X-Ray data collection and structure determination

Diffraction intensities for **1**–**4** were collected on a Bruker APEX-II QUAZAR diffractometer equipped with graphite-monochromated Mo *K*α radiation with a radiation wavelength of 0.71073 Å by using the φ-ω scan technique at 173 (for **1** and **4**) and 296 K (for **2** and **3**), respectively. There was no evidence of crystal decay during data collection. Semiempirical multiscan absorption corrections were applied by SADABS [32] and the program SAINT [33] was used for integration of the diffraction profiles. The structures were solved by direct methods and refined with the full-matrix least-squares technique using the SHELXS-97 and SHELXL-97

programs.[34] Anisotropic thermal parameters were assigned to all non-H atoms. Organic hydrogen atoms were geometrically generated. H atoms attached to water molecule were located from difference maps and refined with isotropic temperature factors. The position of the highest peak in **1** is at (0.3498, 0.1150, 0.7408), 0.90 Å from Cu2, and the position of the deepest hole is at (0.4406, 0.9759, 0.2994), 0.87 Å from Cu2. The position of the highest peak in **2** is at (0.0733, 0.7099, 0.9627), 0.40 Å from N7, and the position of the deepest hole is at (0.0800, 0.4075, 0.5158), 1.03 Å from Cu4. The high residual density of **2** is due to the disorder of the ta^- ligand. The position of the highest peak in **3** is at (0.0000, 0.0000, 0.0000), 1.86 Å from O6, and the position of the deepest hole is at (0.5594, 0.6774, 0.2596), 0.97 Å from Cu6. The possible reason for the high residual density of **3** is due to the crystal defect. Centrosymmetric tp^{2-} and one ta^- ligands in **2** were positionally disordered and varied between two symmetry-related positions with the site occupancy refined to 0.496 and 0.504, as well as 0.737 and 0.263, respectively. One free water molecule (O5) in **2** was also positionally disordered with the site occupancy refined to 0.25. Three O atoms of lattice water molecules (O4 in **2**, as well as O11 and O12 in **3**) were varied between two positions with the site occupancies of 0.51 for O4, 0.53 for O11, 0.46 for O12, as well as 0.49 for O4′, 0.47 for O11′, 0.54 for O12′. No hydrogen atom was located for the disordered water molecule. Crystallographic data and structural refinement were given in Table 1.

/insert Table 1/

Results and discussion

Syntheses and FT-IR spectra

Complexes **1**–**4** were hydrothermally obtained, in which the anions of inorganic metal salt (Cl^- for **1**, NO_3^- for **2** and OAc^- for both **3** and **4**) and pH value (pH = 6) of the mixed medium were found to be more essential for the growth of the targeted crystalline samples. Other anions and higher or lower pH value only

led to amorphous powder or micro-crystals that were structurally different from the target complexes.

In the IR spectra (Fig. S1), broad bands centered around 3400 cm^{-1} in **1–4** are corresponding to the characteristic vibrations of O–H, confirming the existence of hydroxyl group and/or water molecule. Compared with the isolated organic acid, the absence of a band at *ca*. 1686–1730 cm^{-1} suggests the full deprotonation of polycarboxylic acids in **1–4**. The characterized multiple bands corresponding to the asymmetric (ν_{as}) and symmetric (ν_s) stretching vibrations for COO^- are observed between 1600 and 1400 cm^{-1}, and their different separations ($\Delta\nu = \nu_{as} - \nu_s$) suggests the rich coordination modes of the carboxylate groups. Thus, the IR results of **1–4** are in good agreement with the single crystal X-ray diffraction data.

Crystal structures of 1–4

$[Cu_4(\mu\text{-OH})(\mu_3\text{-OH})(ta)_2(btec)]_n$ (1). Complex **1** is an intriguing 3D framework constructed from coplanar Cu^{II}_7 clusters, 4-connected Cu^{II}_1 nodes and 6-connected $btec^{4-}$ connectors, exhibiting a $(4^4\cdot6^2)(4^{11}\cdot6^5)_2(4^{13}\cdot6^{10}\cdot8^5)$ topological network. The asymmetric unit of **1** contains five Cu^{II} ions with Cu4 and Cu5 lying at different inversion centers, two bridging bidentate and tridentate hydroxyl groups, two deprotonated μ_3-N1,N2,N3-ta^- ligands to consolidate the local Cu^{II}_7 cluster and one fully deprotonated $btec^{4-}$ anion. As shown in Fig. 1a, both Cu1 and Cu2 are five-coordinated in distorted square-pyramidal coordination geometries with Addison parameter τ = 0.05 and 0.39, respectively. The τ value is defined as an index of trigonality (τ = 1) and square-pyramid (τ = 0).[35] The apical positions of the both metal ions are occupied by carboxylate O atoms from $btec^{4-}$ ligand, and the basal planes are slightly different (O_3N for Cu1 and N_2O_2 for Cu2). The remaining three Cu^{II} ions are in square-planar coordination geometrywith Cu4 and Cu5 in the different inversion centers and Cu3 ion in a general position. Both Cu3 and Cu4 sites are in a N_2O_2 donor set surrounded by pairs of μ_3-ta^- and bridging hydroxyl groups. While the Cu5 ion is embraced by four carboxylate O atoms from four symmetry-related $btec^{4-}$ ligands. The bond lengths of

Cu–O and Cu–N are between 1.898(4) and 2.352(4) Å (Table S1), comparable with those Cu^{II}-containing complexes with mixed carboxylate and tri- or tetrazolyl ligands.[36] The full deprotonated $btec^{4-}$ ligand in **1** is crystallographically asymmetric and presents four crystallographic independent carboxylate groups to bind seven Cu^{II} ions in a μ_7-κ^7O1:O2:O3:O4:O5:O7:O7 mode (Fig. 2).

/insert Fig. 1 and Fig. 2/

The central Cu4 ion aggregates two pairs of centrosymmetric Cu^{II} ions (Cu2 and Cu2A as well as Cu3 and Cu3A) by two asymmetric μ_3-OH^- groups and two μ_3-N1,N2,N3-ta^- ligands (Fig. 1b), generating a hourglass-shaped $\{Cu_5(\mu_3\text{-}OH)_2(ta)_2\}^{6+}$ precursor. Two additionally centrosymmetric Cu1 and Cu1A ions continue to incorporate into the Cu^{II}_5 precursor by two bridging μ-OH^- groups and another pair of crystallographically independent μ_3-N1,N2,N3-ta^- ligands. As a result, an centrosymmetric Cu^{II}_7 cluster, $\{Cu_7(\mu_3\text{-}OH)_2(\mu\text{-}OH)_2(ta)_4\}^{4+}$, is generated with the intermetallic distances of 3.3935(5), 3.4231(5), 3.3599(5) and 3.2215(6) Å for Cu1···Cu3, Cu2···Cu3, Cu2···Cu4 and Cu3···Cu4, respectively (Fig. 1b). Notably, all the seven Cu^{II} ions with the Cu^{II}_7 cluster are strictly coplanar, suggesting that the co-coordination of hydroxyl group and ta^- is favorable for the Cu^{II}_7 cluster.

The Cu^{II}_7 cluster, the square-planar Cu5 ion and fully deprotonated $btec^{4-}$ anion can act as secondary build blocks to generate the 3D framework of **1**. As illustrated in Fig. 1c, each Cu^{II}_7 cluster in **1** is surrounded by eight $btec^{4-}$ ligands, and can be topologically treated as an eight-connected node. Full deprotonated $btec^{4-}$ anion in **1** links four Cu^{II}_7 clusters and two square-planar Cu5 ions, becoming a six-connected node (Fig. 1c). Instead, the planar-square Cu5 ion is surrounded by four $btec^{4-}$ ligands, serving as a four-connected node. The 8-, 6- and 4-connected nodes in **1** are periodically interconnected together to result in a complicated 3D framework of **1** (Fig. S2), which can be simplified into a 4, 6, 8-trinodal network with a topological symbol of $(4^4\cdot6^2)(4^{11}\cdot6^5)_2(4^{13}\cdot6^{10}\cdot8^5)$ obtained by TOPOS (Fig. 1d).[37]

It should be noted that within the 3D framework, an alternating Cu^{II}_7+Cu^{II}_1 chain is extended by the *syn*, *anti*-COO^- moiety of $btec^{4-}$ ligand (Fig. 1e), which should be responsible for the magnetic interactions of **1**.

$\{[Cu_6(\mu_3\text{-}OH)_2(ta)_8(tp)]\cdot 2.5H_2O\}_n$ (2). Taking place of the $btec^{4-}$ connector by tp^{2-} coligand with less carboxylate groups in the ternary system generated a pillared-layer framework of **2**, which is built from alternating Cu^{II}_5+Cu^{II}_1-based coplanar layers and bi-directional tp^{2-} pillars. The fundamentally structural unit of **2** contains a centrosymmetric $\{Cu_5(\mu_3\text{-}OH)_2(ta)_4\}^{4+}$ subunit, one axially elongated Cu^{II}_1 octahedron, one centrosymmetric tp^{2-} connector with double deprotonation as well as two and a half lattice water molecules. The unique Cu1 and Cu2 ions within the Cu^{II}_5 cluster are five-coordinated in distorted square-pyramidal geometry with τ = 0.36 and 0.09, respectively (Fig. 3a). The basal planes of the both Cu^{II} atoms are well defined by one μ_3-OH^- and three individual N atoms from three different ta^- ligands, and the apical site is occupied by carboxylate O (for Cu1) or triazolyl N (for Cu2) donor. The apical Cu–O or Cu–N bond length is considerably longer by ca. 0.2 Å than those in the basal planes (Table S2). The central Cu3 in the Cu^{II}_5 cluster and the Cu4 outside the Cu^{II}_5 cluster of **2** reside in the different inversion centers, and are in the axially elongated N_4O_2 octahedral surroundings completed by ta^-, μ_3-OH^- and/or carboxylate groups tp^{2-} coligand. The bond lengths of axial Cu–N (for Cu3) and Cu–$O_{carboxylate}$ (for Cu4) are considerable longer by 0.4 Å than those in the equatorial planes (Table S2).

/insert Fig. 3/

A pair of μ_3-OH^- groups aggregate one central Cu3 and two pairs of centrosymmetric Cu1 and Cu1A as well as Cu2 and Cu2A atoms, generating a hourglass-like $\{Cu_5(\mu_3\text{-}OH)_2(ta)_2\}^{6+}$ cluster with the three adjacent metal ions further enhanced by μ_3-N1,N2,N3-ta^- anions (Fig. 3a). Notably, all the metal ions in the Cu^{II}_5 cluster are coplanar and the inter-metallic distances are 3.3923(2), 3.3053(3) and 3.2664(3) Å for

Cu1···Cu2, Cu1···Cu3 and Cu2···Cu3, respectively. Thus, the local Cu^{II}_5 cluster of **2** is much analogous to the precursor in **1**, and also benefits greatly from the co-coordination of the μ_3-ta^- and μ_3-OH^- group towards the Cu^{II} ions.

Each Cu^{II}_5 cluster of **2** are connected together by pairs of the exterior μ_3-ta^- linkers, generating an one-dimensional (1D) chain running along crystallographic *a*-direction with the nearest intercluster Cu^{II}···Cu^{II} distance of 3.5898(3) Å. The neighboring 1D chains join the octahedral Cu^{II}_1 cores through two pairs of ta^- ligands in μ-N1,N2- and μ-N1,N2, N3-manners, affording an infinite two-dimensional (2D) layer (Fig. 3b) with the interchain distance of 3.8077 Å separated by the Cu^{II}_1 core. Behaving as ditopic pillars, the centrosymmetric tp^{2-} ligands extend the adjacent layers in a bis-bidentate bridging mode (μ_4-κ^4 O1:O2:O3:O4-tp^{2-}, Fig. 2), resulting in a pillared-layer framework of **2** (Fig. 3c) with the shortest interlayer distance of *ca* 10.9804(8) Å.

$\{[Cu_5((\mu_3\text{-}OH)_2(ta)_4(ip)_2]\cdot 2H_2O\}_n$ (3). Further pulling the two carboxylate groups of coligand closer to a *meta*-isomer, a grid-like microporous framework of **3** is fabricated with two unique Cu^{II}_5 clusters-based 1D chains interconnected by two different kinds of tritopic ip^{2-} connectors. The fundamentally structural unit of **3** contains two crystallographically independent $\{Cu_5(\mu_3\text{-}OH)_2(ta)_4\}^{4+}$ clusters, two pairs of doubly deprotonated ip^{2-} connectors in μ_3- and μ_4-binding modes (Fig. 2) and four disordered lattice water molecules.

Both the unique Cu^{II}_5 cores in **3** are much similar to that in **2** only with slightly different coordination polyhedra of the central metal ion and one of the five-coordinate Cu^{II} ions (Fig. 4a and Fig. 4b). The central Cu5 ion in the Cu^{II}_5 core of **3** adopts a square-planar coordination geometry completed by N_2O_2 donor set arising from pairs of μ_3-ta^- and μ_3-OH^- groups, which is dramatically different from the N_4O_2 coordination environment of the central Cu3 octahedron of **2**. Additionally, the NO_4 coordination surroundings for the

Cu2 ion of **2** are changed to N_3O_2 donor sets of Cu2 and Cu6 in the Cu^{II}_5 cores of **3**, which means that two carboxylate O atoms instead of two triazolyl N donors to bind with the metal ion (Fig. 4a and Table S3).

/insert Fig. 4/

As shown in Fig. 4c, two unique Cu^{II}_5 cores in **3** are alternately extended into 1D chains by couples of μ_3-ta$^-$ ligands with the nearest intercluster $Cu^{II}\cdots Cu^{II}$ separation of 3.4367(2) Å. Moreover, the adjacent Cu^{II}_5 clusters are perpendicular to each other, which greatly reduce the spatial hindrance of the targeted complex. The Cu^{II}_5 cluster-based 1D chains of **3** are then connected together by pairs of μ_3-ip^{2-} connectors in a μ_3-κ^3 O1:O1:O3-binding mode (Fig. 2), resulting a 2D layer of **3** (Fig. 4c). Notably, the μ_3-ip^{2-} connector in **3** acts as a tritopic node to hold three Cu^{II}_5 clusters together (Fig. S3). The adjacent layer of **3** are further supported by μ_4-ip^{2-} connector in a bis-bidentate bridging mode (μ_4-κ^4 O1:O2:O3:O4-ip^{2-}, Fig. 2) to generate an overall microporous framework of **3** with total potential solvent accessible void volume of 1679.7 Å^3 calculated by PLATON program.[38] The μ_4-ip^{2-} ligand in **3** also serves as a three-connected node despite of its tetradentate binding mode, because it also aggregates three individual Cu^{II}_5 clusters together. Notably, the interchain separations across the two unique ip^{2-} connectors are 5.6646(4) and 5.7471(5) Å, considerable shorter than the interlayer distance of **2** separated by the *para*-isomeric coligand. The 3D framework of **3** can be topologically predigested as a 3,3,8,8-tetranodal net with a topological symbol of $(3\cdot4^2)_2(4^2\cdot6)_2(3^2\cdot4^4\cdot5^2\cdot6^{10}\cdot7^6\cdot8^2\cdot9\ 10)(3^2\cdot4^4\cdot5^4\cdot6^6\cdot7^6\cdot8^5\cdot9)$ (Fig. 4d).

$\{[Cu_5(\mu\text{-}OH)_2(\mu_3\text{-}OH)_2(ta)_2(pa)_2]\cdot2H_2O\}_n$ (4). Complex **4** crystallizes in the triclinic $P\bar{1}$ space group, exhibiting an undulated 2D layer with centrosymmetric $\{Cu_4(\mu_3\text{-}OH)_2\}^{6+}$ and square-planar Cu^{II}_1 subunits alternatively propagated by anionic pa^{2-} and μ_3-ta$^-$ connectors. The asymmetric unit of **4** contains two and a half crystallographically independent Cu^{II} ions, two bridging μ- and μ_3-OH$^-$ groups, one μ_3-N1,N2,N3-ta$^-$ anion, one doubly deprotonated pa^{2-} coligand as well as one free water molecule. Located at general

positions, both Cu1 and Cu2 ions in **4** are in the NO_4 donor sets (Fig. 5a), displaying slightly distorted square-pyramid with τ = 0.01 and 0.16. The basal planes of Cu1 site is well-defined by two hydroxyl groups, one carboxylate O and one triazolyl N donors, and the apical site is fulfilled by one carboxylate O atom from one pa^{2-} anion. Instead, the basal sites of the Cu2 ion are generated by one μ_3-OH^- group, two separate carboxylate O donors from two different pa^{2-} anions and one N atom from ta^- ligand, and the apical position is fulfilled by one μ_3-OH^- group. The apical Cu–O distances are considerable longer by 0.7 and 0.3 Å than those of equatorial Cu–O and Cu–N bonds (Table S4). Locating at an inversion center, the unique Cu3 ion in **4** is in a square-planar coordination geometry completed by two N and two O donors from a pair of symmetry-related μ_3-ta^- ligand and two μ-OH^- groups.

/insert Fig. 5/

Acting as an asymmetric tridentate bridge, a pair of μ_3-OH^- groups aggregate four centrosymmetric Cu^{II} ions from two adjacent asymmetric units, generating a butterfly-shaped $\{Cu_4(\mu_3\text{-}OH)_2\}^{6+}$ core with the intermetallic distance of 3.1186(2), 3.3879(2) and 3.1919(2) Å for Cu1···Cu2, Cu1···Cu2A and Cu2···Cu2A, respectively. The $\angle CuO_{hydroxyl}Cu$ is 122.884(3)°, 95.832(3)° and 98.186(3) ° for ∠Cu1O6Cu2A, ∠Cu1O6Cu2 and ∠Cu2O6Cu2A, which are important parameters for the magnetic couplings of **4**. The butterfly-shaped Cu^{II}_4 clusters in **4** are alternating connected with the square-planar Cu3 ions through pairs of μ-OH^- and μ_3-N1,N2,N3-ta^- ligands, affording an infinite 1D wavy chain running along [1 1 0] direction (Fig. 5b). The shortest distance between Cu^{II}_4 and Cu^{II}_1 by μ-OH^- group is 3.3364 (2) Å. The alternating Cu^{II}_4+Cu^{II}_1 chain can be previously observed in the 1,2,4-triazolate-based framework.[36] Furthermore, each Cu^{II}_4+Cu^{II}_1 chain of **4** is interconnected together through μ_4-pa^{2-} ligands in a bidentate bridging and single-atom bridging mode (μ_4-κ^4 O1:O2:O3:O3-pa^{2-}, Fig. 2) to lead to an infinite 2D layer of **4** (Fig. 5b). The shortest interchain distance by the μ_4-pa^{2-} connector is *ca* 5.2587(4)

Å, considerable shorter than those of **2** and **3** constructed from the *para*- and *meta*-isomers. In addition, the adjacent layers of **4** can be further stacked into a non-covalent 3D network by interlayer π···π stacking interactions between the adjacent phenyl rings with center-to-center distance of 3.5912(2) Å (Fig. S4).

The above structural analyses of **1**−**4** clearly indicate that the increase of the nuclearity from centrosymmetric Cu^{II}_4 to Cu^{II}_7 greatly benefits from the cooperative co-coordination of the hydroxyl group and 1,2,3-triazolate ligand to metal ion under hydrothermal conditions. In addition to the well matched intermetallic distance for the μ_3-/μ-OH^- and μ_3-/μ-ta^-, the stabilized five-membered chelate ring of Cu2N2O is also an important factor for the formation of the clusters. By contrast, the extension of the dimensionality from 2D layer to 3D framework depends significantly on the carboxylate moieties, in which the isomerism of the two carboxylate groups towards the phenyl spacer controls the interchain/interlayer compactability. Thus, the *ortho*-, *meta*- and *para*-isomers of the dicarboxylate coligands made the interchain or interlayer distances of 5.26, 5.71 and 10.98 Å. Therefore, the core-expansion and skeleton compactness are successfully achieved by subtle manipulations of the hydrothermal self-assembly process of the 1,2,3-triozolate and Cu^{II} salts in the presence of polycarboxylate coligands.

TG and PXRD results

TGA experiments (Fig. S5) indicated that **1** without any lattice molecules can be thermally stable up to 304 ^oC and was followed by an obvious weight-loss stage till 345 ^oC for the collapse of the complicated 3D framework. Notably, the backbone collapse of **1** was not completely finished at the highest temperature measured. By contrast, samples **2**–**4** exhibited two separate weight-loss processes. The first one observed between 50 and 140 °C (for **2** and **3**) and between 25 and 90 °C (for **4**) was due to the removal of lattice water molecules (obsd. 3.8%, calcd. 3.9% for **2**, obsd. 3.8%, calcd. 3.6% for **3** and obsd. 4.1%, calcd. 4.9% for **4**). Once the temperature was higher than 290 ^oC, the weight of **2** decreased abruptly because of the

explosion. Differently, an apparent weight-loss stage of **3** for the broken of the framework was clearly detected between 290 and 410 °C, which was not totally finished similar to **1**. The second weight-loss stage of **4** started at 292 °C and ended at 370 °C, corresponding to the decomposition of the mixed ligands and the broken of the framework. The final residue of **4** was calculated to be CuO (obsd. 43.7%, calcd. 44.9%). PXRD pattern was used to check the phase purity and structural consistency of the bulky samples. As a result, the measured PXRD patterns of **1–4** matched well with the simulated ones generated from the results of single-crystal diffraction data (Fig. S6).

Magnetic properties

Variable-temperature (2–300 K) magnetic susceptibilities of **1**–**4** were measured on the crystalline samples under an applied direct-current (dc) field of 1.0 kOe. The $\chi_M T$ product per Cu^{II}_7+Cu^{II}_1 subunit of **1** is 2.48 cm^3 K mol^{-1} at 300 K (Fig. 6a), which is moderately lower than the theoretical value (3.00 cm^3 K mol^{-1}) expected for eight magnetically isolated Cu^{II} ions with $S = 1/2$ and $g = 2.0$. The $\chi_M T$ value decreases rapidly with the decreasing temperature and reaches a local minimum of 1.05 cm^3 K mol^{-1} at 30.0 K due to the strong antiferromagnetic couplings between the adjacent spin carriers. Then, the $\chi_M T$ value increases abrupt and reaches a value of 2.03 cm^3 K mol^{-1} at 2.0 K, suggesting possibly intercluster ferromagnetic interactions. To quantitatively evaluate the coupling strength between the adjacent spin carriers, an approximate heptanuclear model with spin Hamiltonian $\boldsymbol{H} = -J_1(\boldsymbol{S}_{Cu1}\boldsymbol{S}_{Cu3}+\boldsymbol{S}_{Cu3A}\boldsymbol{S}_{Cu1A}+\boldsymbol{S}_{Cu3}\boldsymbol{S}_{Cu4}+\boldsymbol{S}_{Cu4}\boldsymbol{S}_{Cu3A}+\boldsymbol{S}_{Cu2A}\boldsymbol{S}_{Cu3}+\boldsymbol{S}_{Cu3A}\boldsymbol{S}_{Cu2}+\boldsymbol{S}_{Cu2}\boldsymbol{S}_{Cu4}+\boldsymbol{S}_{Cu2A}\boldsymbol{S}_{Cu4})-J_2(\boldsymbol{S}_{Cu1}\boldsymbol{S}_{Cu2A}+\boldsymbol{S}_{Cu1A}\boldsymbol{S}_{Cu2}+\boldsymbol{S}_{Cu2}\boldsymbol{S}_{Cu3}+\boldsymbol{S}_{Cu2A}\boldsymbol{S}_{Cu3A})+\boldsymbol{S}_{Cu5}$ is used to fit the experimental magnetic susceptibilities of **1**, in which J_1 and J_2 roughly describe the intracluster magnetic couplings (Table S5 and Fig. 6a inset) and the contribution from the individual Cu5 ion is considered as an isolate Curie-like paramagnetic centre. The least-squares fitting of the magnetic data of **1** above 30.0 K by MAGPACK suite[39] leads to $g = 2.12$, $J_1 =$

–127.1 cm^{-1}, J_2 = –21.4 cm^{-1} and R = 8.2 × 10^{-4}, where R is agreement factor defined as $\Sigma[(\chi_M T)_{obsd}-(\chi_M T)_{calcd}]^2/\Sigma[(\chi_M T)_{obsd}]$. Obviously, the strong antiferromagnetic interaction for J_1 should be assigned to the superexchange pathways by basal and/or equatorial hydroxyl and –NN– of μ_3-tz^- heterobridges. Moreover, the bigger bond angles of ∠CuNN and ∠CuOCu (Table S5) can further increase the overlap of the magnetic orbits from the Cu^{II} ions and hydroxyl group/μ_3-tz^- mediators to enhance the antiferromagnetic interaction. By contrast, the small J_2 is associated with the relatively long intermetallic distances separated by the –NCN– moiety of μ_3-tz^- ligand.

Isothermal magnetization of **1** measured at 2.0 K (Fig. 6b) increases with the enhanced magnetic field and reaches slowly the saturation value of 2.03 $N\beta$ at 70 kOe. Moreover, the experimental M–H curve is above the theoretical Brillouin function for S = 1 and g = 2.0, suggesting weak intercluster ferromagnetic interactions. The saturated magnetization for each Cu^{II}_7+Cu^{II}_1 subunit of **1** at 70 kOe is in good agreement with the susceptibility data (2.00 $N\beta$) for two Cu^{II} ions with S = 1/2 and g = 2.0, confirming that S = 1 spin ground-state of **1** is generated at low temperature. Obviously, spin ground-state of **1** comes from the weak ferromagnetic coupling of the Cu^{II}_1 and the net magnetization produced in the antiferromagnetic coupled Cu^{II}_7 cluster, which is mediated by the *syn*, *anti*-COO^- bridge.

Different form paramagnetic behavior of **1**, the hourglass-shaped Cu^{II}_5 cluster-based **2** and **3** exhibit spin-canted antiferromagnetism and ferrimagnetism, respectively. The room-temperature $\chi_M T$ value for each Cu^{II}_5+Cu^{II}_1 subunit of **2** (1.83 cm^3 K mol^{-1}) is only slightly smaller than that (2.00 cm^3 K mol^{-1}) for per Cu^{II}_5 subunit of **3**, implying stronger inter-/intra-cluster antiferromagnetic coupling of **2** than **3** even at ambient temperature. The stronger antiferromagnetic interaction of **2** than **3** can also be concluded by comparisons of the Weiss constants (–267 vs –166 K) of the Curie-Weiss fitting above 110.0 K (Fig. S7). Upon cooling, the both $\chi_M T$ values decreases continuously and reaches minimums at 18.0 (for **2**) and 16.0

K (for **3**). Then, the $\chi_M T$ shows abruptly rise upon further cooling, suggesting the onset of magnetic ordering with a spontaneous magnetization. The final drop of $\chi_M T$ of **2** may due to the inter-layer antiferromagnetic interactions. Both the χ_M–T curves of **2** and **3** are field-dependent at low temperature (Fig. S8).

Isothermal magnetization of **2** measured at 2.0 K (Fig. 6b) shows an initially abrupt increase with the fields below 5 kOe. Then, it increases linearly with the increasing field and gets to 0.18 $N\beta$ at 70 kOe, which is less than the expected value (1.0 $N\beta$) for one Cu^{II} ion, implying that **2** serves as a canted antiferromagnet arising from the asymmetric magnetic pathway mediated by –NNN– moiety of μ_3-ta$^-$ anion in the isotropic Cu^{II}_5+ Cu^{II}_1-based 2D sublayer. By contrast, the magnetization for per Cu^{II}_5 subunit of **3** increases quickly with the increasing field and is obviously far from Brillouin law for S = 1/2 and g = 2.0. The magnetization per Cu^{II}_5 unit of **3** is 1.01 $N\beta$ at 70 kOe, confirming the ferrimagnetic behavior of **3** to lead to S = 1/2 spin ground-state at low temperature. The ferrimagnetism of **3** is arising from the ordering arrangement of the net magnetization of the antiferromagnetically coupled Cu^{II}_5 clusters in the local 2D layer of **3** by the carboxylate of ip^{2-} ligand.

Alternating-current (ac) susceptibilities were measured to investigate the magnetic dynamic of **2** and **3**. Both the in-phase (χ') and out-of-phase (χ'') components slowly rise with the decreasing temperature and reach a maximum at 2.0 K without an obvious peak (Fig. 7), suggesting that the Néel temperature (T_N) of **2** and **3** is lower than 2.0 K. The lowered T_N of the two samples can also be evidence by the identical zero-field-cool (ZFC) and field-cool (FC) plots down to 2.0 K, which may be due to the spin frustration by the hourglass-like arrangement of the spin carriers in local Cu^{II}_5 clusters.[40] Additionally, the ac susceptibilities are frequency-independent, precluding the possibility of a spin-glass behavior.[41]

The room temperature $\chi_M T$ value for each Cu^{II}_4+Cu^{II}_1 subunit of **4** is 1.38 cm^3 K mol^{-1} (Fig. 6a), lower

than the value for five Cu^{II} ions with $S = 1/2$ and $g = 2.0$. Upon cooling, the $\chi_M T$ quickly drops to 0.39 cm^3 K mol^{-1} at 2.0 K resulting from the strong antiferromagnetic couplings between the adjacent Cu^{II} spins. The $\chi_M T$ product of **4** at low temperature is very close to 0.375 cm^3 K mol^{-1} corresponding to the $S = 1/2$ spin ground-state, indicating that there is one unpaired *d* electron within the Cu^{II}_4+Cu^{II}_1 chain. Obviously, the Cu^{II}_1 core is the origin for the spin ground state because the antiferromagnetically coupled Cu^{II}_4 cluster lead to a zero magnetization. The magnetization of **4** performed at 2.0 K follows roughly a Brillouin function with $S = 1/2$ and $g = 2.0$, and the saturation value (1.03 $N\beta$) corresponding to one unpaired *d* electron is reached at 70 kOe. Thus, the layered sample **4** with Cu^{II}_4+Cu^{II}_1 motif exhibit a paramagnetic S=1/2 spin ground-state at low temperature.

Conclusion

Hydrothermal reactions of Cu^{II} source, 1,2,3-triazole and carboxylate-modified coligands provide centrosymmetric Cu^{II}_7, Cu^{II}_5, Cu^{II}_4 and Cu^{II}_1 motifs with different core topologies, which are further extended into three 3D frameworks and 2D layer with tunable interchain/interlayer compactness. The expansion of the nuclearities from four to seven is crystallographically resulting from co-coordination of the 1,2,3-triazolate and hydroxyl group towards the metal ion, and the substitution isomerism of the dicarboxylate groups from the coligand essentially triggers a noticeable interchain and interlayer compactness. Due to the antiferromagnetic couplings in the local clusters and the asymmetric magnetic exchange by 1,2,3-triazolate, these complexes exhibit paramagnetic $S = 1$ and 1/2, ferrimagnetic $S = 1/2$ as well as canted antiferromagnetic behaviors at low temperature.

Acknowledgements

This present work was financially supported by the National Natural Science Foundation of China (Grants 21171129, 21173157 and 21371134), the 973 Program (2014CB845601), the Program of Innovative

Research Team in University of Tianjin (TD12−5038), and Tianjin Municipal Education Commission (2012ZD02), which are gratefully acknowledged.

References

1 T. R. Cook, Y. R. Zheng and P. J. Stang, *Chem. Rev*., 2013, **113**, 734.

2 W. C. Song, Q. H. Pan, P. C. Song, Q. Zhao, Y. F. Zeng, T. L. Hu and X. H. Bu, *Chem. Commun.,* 2010, **46**, 4890.

3 Y. B. Zhang, W. X. Zhang, F. Y. Feng, J. P. Zhang and X. M. Chen, *Angew. Chem. Int. Ed*., 2009, **48**, 5287.

4 Y. Liu, K. Mo and Y. Cui, *Inorg. Chem*., 2013, **52**, 10286.

5 L. Ma, D. J. Mihalcik and W. B. Lin, *J. A. Chem. Soc*., 2009, **131**, 4610.

6 V. Venkatesh, P. Pachfule, R. Banerjee and S. Verma, *Chem. Eur. J*., 2014, **20**, 12262.

7 J. Li, Y. Guo, H. R. Fu, J. Zhang, R. B. Huang, L. S. Zheng and J. Tao, *Chem. Commun.,* 2014, **50**, 9161.

8 J. B. Peng, Q. C. Zhang, X. J. Kong, Y. Z. Zheng, Y. P. Ren, L. S. Long, R. B. Huang, L. S. Zheng and Z. P. Zheng, *J. Am. Chem. Soc*., 2012, **134**, 3314.

9 P. Q. Liao, X. Y. Li, J. Bai, C. T. He, D. D. Zhou, W. X. Zhang, J. P. Zhang and X. M. Chen, *Chem. Eur. J.,* 2014, **20**, 11303.

10 G. A. Senchyk, A. B. Lysenko, A. A. Babaryk, E. B. Rusanov, H. Krautscheid, P. Neves, A. A. Valente, I. S. Gonçalves, K. W. Krämer, S. X. Liu, S. Decurtins and K. V. Domasevitch, *Inorg. Chem*., 2014, **53** 10112.

11 S. D. Han, J. P. Zhao, Y. Q. Chen, S. J. Liu, X. H. Miao, T. L. Hu and X. H. Bu, *Cryst. Growth Des*., 2014, **14**, 2.

12 W. Ouellette, S. Jones and J. Zubieta, *CrystEngComm*., 2011, **13**, 4457.

13 M. J. Zaworotko, *Angew. Chem. Int. Ed.,* 2000, **39**, 3052.

14 E. C. Yang, Z. Y. Liu, X. Y. Wu and X. J. Zhao, *Chem. Commun.,* 2011, **47**, 8629.

15 P. DeBurgomaster, A. Aldous, H. X. Liu, C. J. O'Conno and J. Zubieta, *Cryst. Growth Des*., 2010, **10**, 2209.

16 M. Y. Wu, F. L. Jiang, X. J. Kong, D. Q. Yuan, L. S. Long and M. C. Hong, *Chem. Sci.,* 2013, **4**, 3104.

17 J. D. Leng, S. K. Xing, R. Herchel, J. L. Liu and M. L. Tong, *Inorg. Chem*., 2014, **53**, 5458.

18 S. I. Vasylevs'kyy, G. A. Senchyk, A. B. Lysenko, E. B. Rusanov, A. N. Chernega, J. Jeziersk, H. Krautscheid, K. V. Domasevitch and A. Ozarowski, *Inorg. Chem*., 2014, **53**, 3642.

19 E. C. Yang, Y. Y. Zhang, Z. Y. Liu and X. J. Zhao, *Inorg. Chem*., 2014, **53**, 327.

20 X. H. Zhou, Y. H. Peng, X. D. Du, J. L. Zuo and X. Z. You, *CrystEngComm*., 2009, **11**, 1964.

21 Y. Y. Liu, M. Grzywa, M. Tonigold, G. Sastre, T. Schüttrigkeit, N. S. Leesondand and D. Volkmer, *Dalton Trans*., 2011, **40**, 5926.

22 M. Grzywa, D. Denysenko, J. Hanss, E. W. Scheidt, W. Scherer, M. Weilc and D. Volkmer, *Dalton Trans*., 2012, **41**, 4239.

23 R. Shaw, R. H. Laye, L. F. Jones, D. M. Low, C. Talbot–Eeckelaers, Q. Wei, C. J. Milios, S. Teat, M. Helliwell, J. Raftery, M. Evangelisti, M. Affronte, D. Collison, E. K. Brechin and E. J. L. McInnes, *Inorg. Chem*., 2007, **46**, 4968.

24 D. C. Zhong, J. H. Deng, X. Z. Luo, X. J. Liu, J. L. Zhong, K. J. Wang and T. B. Lu, *Cryst. Growth*

Des., 2012, **12**, 1992.

25 C. Z. Ruan, R. Wen, M. X. Liang, X. J. Kong, Y. P. Ren, L. S. Long, R. B. Huang and L. S. Zheng, *Inorg*. *Chem*., 2012, **51**, 7587.

26 X. L.Wang, C. Qin, S. X. Wu, K. Z. Shao, Y. Q. Lan, S. Wang, D. X. Zhu, Z. M. Su and E. B. Wang, *Angew. Chem. Int. Ed.,* 2009, **48**, 5291.

27 Y. L. Bai, J. Tao, R. B. Huang and L. S. Zheng, *Angew. Chem. Int. Ed*., 2008, **47**, 5344.

28 E. C. Yang, H. K. Zhao, B. Ding, X. G. Wang and X. J. Zhao, *Cryst. Growth Des*., 2007, **7**, 2009.

29 J. Xiao, B. Y. Liu, G. Wei and X. C. Huang, *Inorg. Chem*., 2011, **50**, 11032.

30 E. C. Yang, Z. Y. Liu, X. J. Shi, Q. Q. Liang and X. J. Zhao, *Inorg. Chem*., 2010, **49**, 7969.

31 W. H. Fang and G. Y. Yang, *Inorg. Chem*., 2014, **53**, 5631.

32 G. M. Sheldrick, *SADABS*, University of Göttingen, Göttingen, Germany, 1996.

33 Bruker AXS, *SAINT software Reference Manual*, Madison, WI, 1998.

34 (*a*) G. M. Sheldrick, *SHELXL–97, Program for X–ray Crystal Structure Refinement*; Göttingen University: Göttingen, Germany, 1997; (*b*) G. M. Sheldrick, *SHELXS–97, Program for X–ray Crystal Structure Solution*; Göttingen University: Göttingen, Germany, 1997.

35 A. W. Addison, T. N. Rao, J. Reedijk, J. V. Rijn and G. C. Verschoor, *J. Chem. Soc. Dalton Trans.*, 1984, 1349.

36 (*a*) E. C. Yang, B. Ding, Z. Y. Liu, Y. L. Yang and X. J. Zhao, *Cryst. Growth Des*., 2012, **12**, 1185; (*b*) E. C. Yang, Y. L. Yang, Z. Y. Liu, K. S. Liu, X. Y. Wu and X. J. Zhao. *CrystEngComm*., 2011, **13**, 2667.

37 V. A. Blatov and A. P. Shevchenko, *TOPOS 4.0*, Samara State University, Russia, 2008.

38 P. van der Sluis and A. L. Spek, *Acta Crystallogr.*, *Sect. A*. 1990, **46**, 194.

39 (*a*) J. J. Borrás-Almenar, J. M. Clemente-Juan, E. Coronado and B. S. Tsukerblat, *Inorg. Chem.*, 1999, **38**, 6081; (*b*) J. J. Borrás-Almenar, J. M. Clemente-Juan, E. Coronado and B. S. Tsukerblat, *J. Comput. Chem.*, 2001, **22**, 985.

40 A. P. Ramirez, *Annu. Rev. Mater. Sci.*, 1994, **24**, 453.

41 J. A. Mydosh, *Spin Glasses: An Experimental Introduction*, Taylor and Francis: London, 1993.

Table 1 Crystal data and structure refinement for **1 – 4** [a]

	1	**2**	**3**	**4**
Chemical formula	$C_{14}H_8Cu_4N_6O_{10}$	$C_{24}H_{27}Cu_6N_{24}O_{8.5}$	$C_{24}H_{22}Cu_5N_{12}O_{12}$	$C_{20}H_{20}Cu_5N_6O_{14}$
F_w	674.42	1168.94	988.24	886.12
Cryst size (mm)	0.15 × 0.14 × 0.13	0.18 × 0.17 × 0.15	0.13 × 0.12 × 0.11	0.18 × 0.17 × 0.15
Cryst syst	Triclinic	Triclinic	Triclinic	Triclinic
Space group	$P\bar{1}$	$P\bar{1}$	$P\bar{1}$	$P\bar{1}$
a (Å)	7.843(2)	8.6725(9)	10.5526(10)	8.3870(6)
b (Å)	9.986(2)	8.8145(9)	10.8749(10)	8.4427(7)
c (Å)	12.320(3)	13.3980(13)	15.3643(14)	10.0939(8)
α (deg)	67.609(4)	78.991(2)	76.545(2)	113.9400(10)
β (deg)	78.650(3)	73.520(2)	82.101(2)	94.1230(10)
γ (deg)	68.577(4)	82.909(2)	79.927(2)	95.5090(10)
V (Å^3)	828.7(3)	961.43(17)	1679.7(3)	645.39(9)
Z	2	1	2	1
D_c (g cm^{-3})	2.703	2.019	1.954	2.280
F(000)	660	581	982	439
μ (mm^{-1})	5.148	3.341	3.193	4.139
Reflections collected / unique	4045 / 2881	5503 / 3361	9408 / 5894	3339 / 2253
R_{int}	0.0349	0.0266	0.0366	0.0108
Data / restraints / params	2881 / 18 / 310	3361 / 44 / 307	5894 / 0 / 489	2253 / 0 / 205
R_1 [a], wR_2 [b] [$I > 2\sigma(I)$]	0.0422 / 0.1054	0.0450 / 0.0921	0.0466 / 0.0814	0.0219 / 0.0540
R_1, wR_2 [all data]	0.0523 / 0.1126	0.0629 / 0.1021	0.0856 / 0.0916	0.0243 / 0.0553
Max. and min. transmission	0.5542 and 0.5123	0.6341 and 0.5846	0.7203 and 0.6816	0.5756 and 0.5229
GOF on F^2	1.043	1.043	1.002	1.055
$\Delta\rho_{max}$, $\Delta\rho_{min}$ / e·Å^{-3}	1.890, – 1.373	1.030, – 1.261	2.318, – 0.580	0.458, – 0.337

[a] $R_1 = \Sigma||F_o|-|F_c||/|F_o|$. [b] $wR_2 = [\Sigma w(|F_o^2|-|F_c^2|)^2/\Sigma w(|F_o^2|)^2]^{1/2}$.

Captions to Figures

Fig. 1 (a) Local coordination environments of Cu^{II} atoms in **1** (Displacement ellipsoids were drawn at the 50% probability level. H atoms and part of phenyl moiety of $btec^{4-}$ were omitted for clarity, symmetry codes: A = 1 – *x*, 1 – *y*, 2 – *z*; B = *x* + 1, *y*, *z*; C = 3 – *x*, 2 – *y*, 2 – *z*; D = 1+ *x*, *y*, 1 + *z*. E = 2 – *x*, 2 – *y*, 2 – *z*; F = 1 – *x*, 1 – *y*, 1 – *z*; G = 2 –*x*, 1 – *y*, 1 – *z*). (b) Coplanar Cu^{II}_7 subunit of **1**. (c) Connections of Cu^{II}_7 cluster, Cu^{II}_1, and $btec^{4-}$ ligand. (d) The (4, 6, 8)-connected topological net of **1**. (e) 1D magnetic chain in **1**.

Fig. 2 Coordination modes of ta^- and carboxylate-functionalized coligands in **1**–**4**.

Fig. 3 (a) Local coordination environments of Cu^{II} atoms in **2** (Displacement ellipsoids were drawn at the 50% probability level. H atoms and part of phenyl moiety of tp^{2-} were omitted for clarity, symmetry codes: A = – *x*, *y* + 1, – *z*; B = 1 – *x*, 1 – *y*, – *z*; C = – *x*, 1 – *y*, 1 – *z*). (b) 2D layer of **2** with Cu^{II}_5 core and Cu^{II}_1 octahedra extended by μ_3-ta^- connectors. (c) Pillared-layer framework of **2**.

Fig. 4 (a) Local coordination environments of Cu^{II} atoms in **3** (Displacement ellipsoids were drawn at the 50% probability level. H atoms and part of phenyl moiety of ip^{2-} were omitted for clarity, symmetry codes: A = – *x*, 2 – *y*, – *z*; B = – *x*, 1 – *y*, – *z*; C = 1 – *x*, 1 – *y*, 1 – *z*; D = *x* + 1, *y*, *z*; E = 1 – *x*, 2 – *y*, – *z*). (b) Superposition diagram of two local Cu^{II}_5 clusters in **3**. (c) 2D layer of **3** with Cu^{II}_5 clusters extended by ta^- and ip^{2-} connectors. (d) 3D framework and the topological representation of **3**.

Fig. 5 (a) Local coordination environments of Cu^{II} atoms in **4** (Displacement ellipsoids were drawn at the 50% probability level. H atoms were omitted for clarity, symmetry codes: A = – *x*, – *y*, 1 – *z*; B = 1 – *x*, 1 – *y*, 1 – *z*; C = 1 – *x*, – *y*, 1 – *z*). (b) 2D layer of **4** with Cu^{II}_4 and Cu^{II}_1 subunits extended by pa^{2-} and μ_3-ta^- connectors.

Fig. 6 (a) Temperature dependence of $\chi_M T$ for **1**–**4** (Solid line represents the best least-squares fit indicated in the text). (b) Isothermal magnetization for **1**–**4** measured at 2.0 K (The dashed lines represent the Brillouin functions respectively for $S = 1/2$, $g = 2.0$ and $S = 1$, $g = 2.0$).

Fig. 7 FC (□) and ZFC (■) magnetizations for **2** and **3** (Inset: χ' and χ'' ac magnetic susceptibilities in zero dc field and in an ac field of 3.5 Oe at different frequencies).

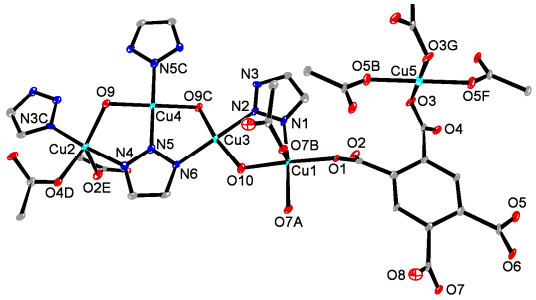

(a)

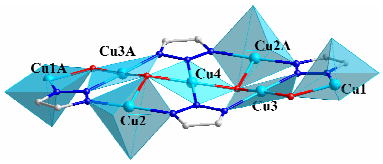

(b)

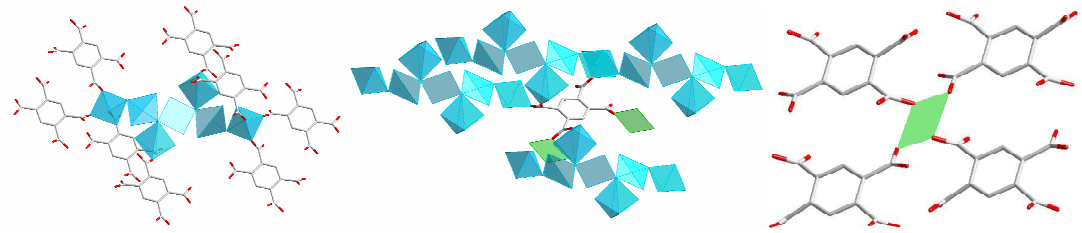

8-connected Cu^{II}_7 cluster

6-connected $btec^{4-}$ connector

4-connected Cu^{II}_1

(c)

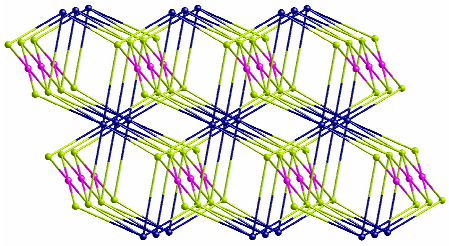

= $\{Cu_7(\mu_3\text{-}OH)_2(\mu\text{-}OH)_2(ta)_4\}^{4+}$
= $btec^{4-}$
= Cu^{II}_1

(d)

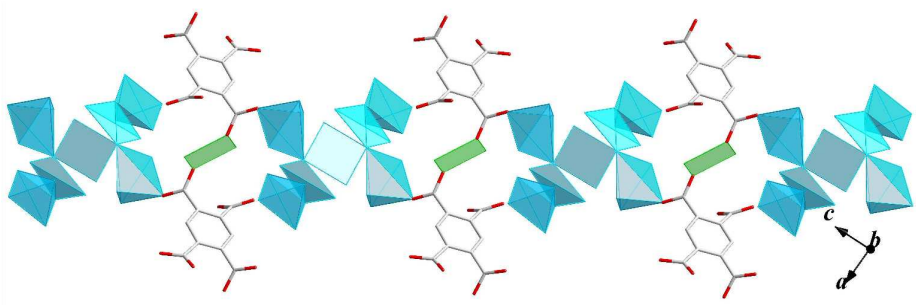

(e)

Fig. 1

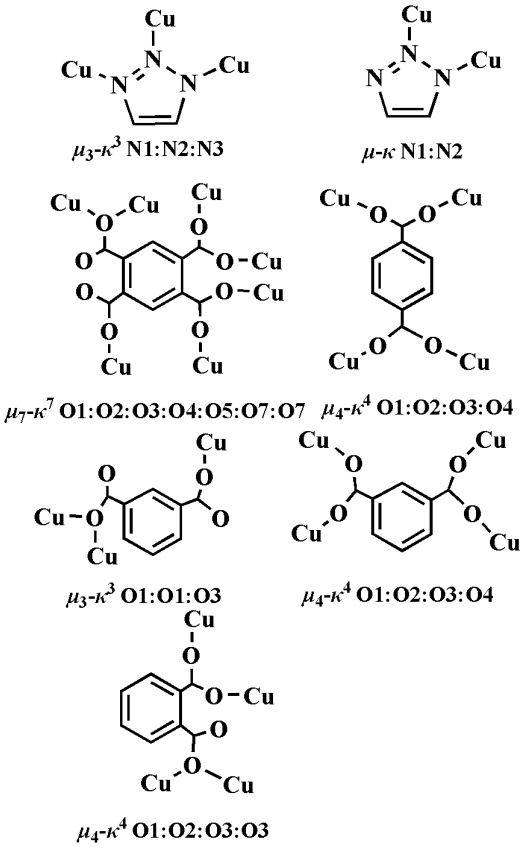

Fig. 2

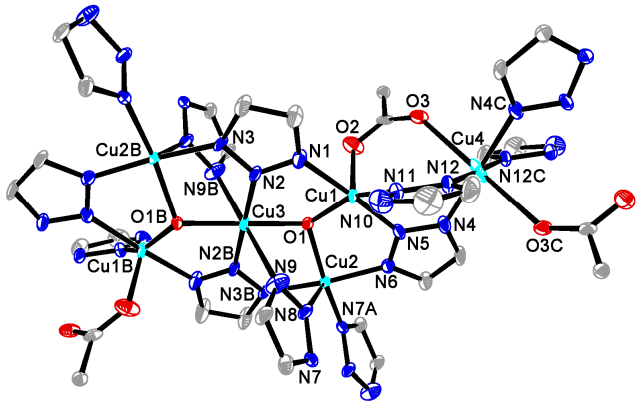

(a)

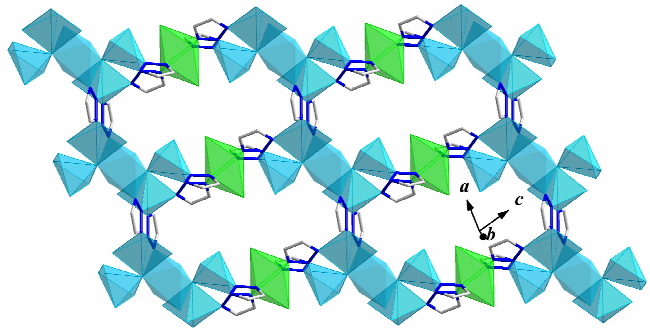

(b)

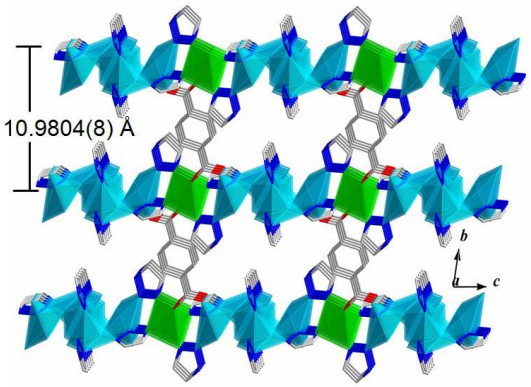

(c)

Fig. 3

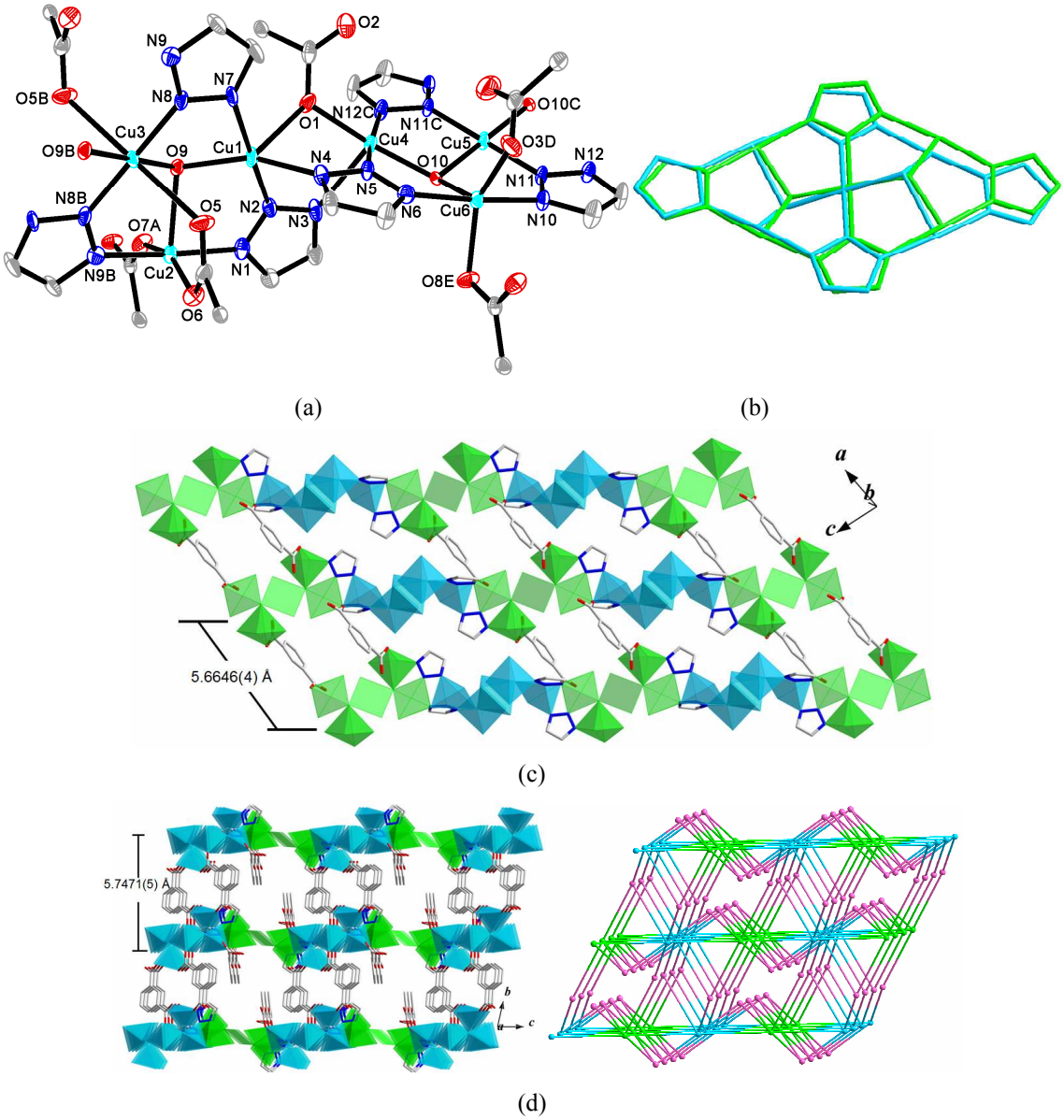

Fig. 4

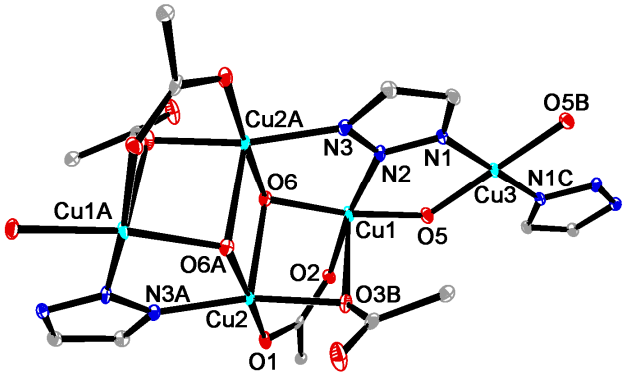

(a)

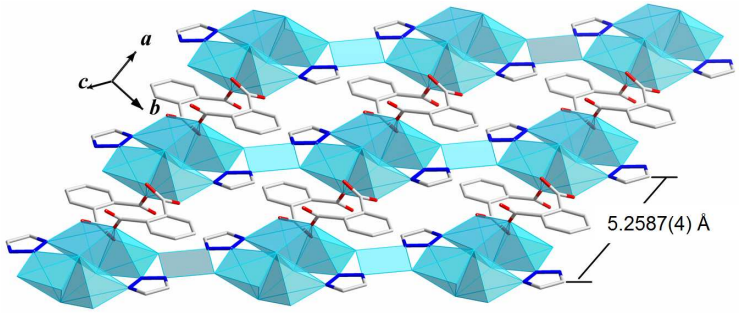

(b)

Fig. 5

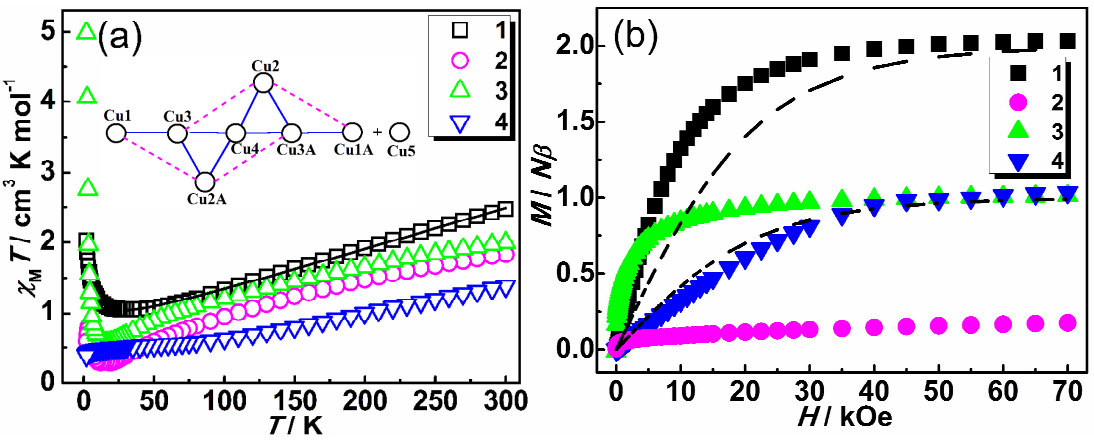

Fig. 6

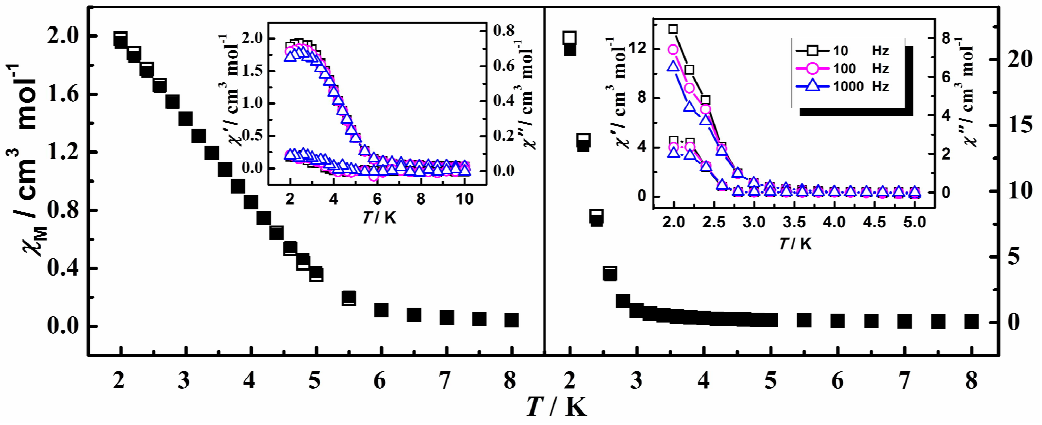

Fig. 7

Table of Content

Triazolate-based 3D frameworks and 2D layer with centrosymmetric Cu^{II}_7, Cu^{II}_5, Cu^{II}_4 clusters and tunable interlayer/interchain compactness: Hydrothermal syntheses, crystal structures and magnetic properties

Yuan-Yuan Zhang,[a] Hong Zhao,[a] En-Cui Yang,[a,*] Zhong-Yi Liu,[a] Qiu Shang[a] and Xiao-Jun Zhao [a,b*]

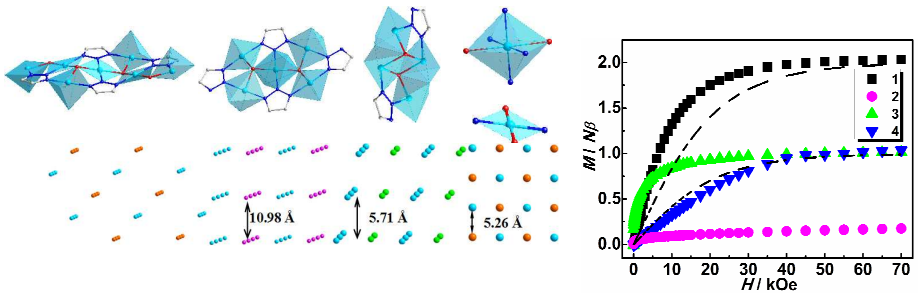

Synergistic co-coordination of hydroxyl group and 1,2,3-triazolate towards Cu^{II} ion generated centrosymmetric Cu^{II}_n (n = 1, 4, 5 and 7) subunits, which were further assembled into 2D layer and 3D frameworks with different interchain and interlayer compactness and spin ground-states at low temperature.